

See discussions, stats, and author profiles for this publication at: <https://www.researchgate.net/publication/320477164>

# Controlling Cu<sub>2</sub>ZnSnS<sub>4</sub> (CZTS) phase in microwave solvothermal synthesis

Article in *Journal of Materials Chemistry A* · October 2017

DOI: 10.1039/C7TA06086F

CITATIONS

0

READS

48

6 authors, including:



Alexandre Henrique Pinto

Ithaca College

7 PUBLICATIONS 33 CITATIONS

[SEE PROFILE](#)



Seung Wook Shin

University of Toledo

108 PUBLICATIONS 1,968 CITATIONS

[SEE PROFILE](#)



Eray Aydil

University of Minnesota Twin Cities

229 PUBLICATIONS 10,571 CITATIONS

[SEE PROFILE](#)

Some of the authors of this publication are also working on these related projects:



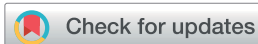
Current project. [View project](#)



Low-k dielectric materials [View project](#)

All content following this page was uploaded by [Seung Wook Shin](#) on 14 November 2017.

The user has requested enhancement of the downloaded file.



Cite this: DOI: 10.1039/c7ta06086f

## Controlling Cu<sub>2</sub>ZnSnS<sub>4</sub> (CZTS) phase in microwave solvothermal synthesis†

Alexandre H. Pinto,<sup>‡\*a</sup> Seung Wook Shin,<sup>§b</sup> Elianna Isaac,<sup>¶a</sup>  
Theodore R. Knutson,<sup>a</sup> Eray S. Aydil<sup>‡\*b</sup> and R. Lee Penn<sup>¶\*a</sup>

The semiconductor Cu<sub>2</sub>ZnSnS<sub>4</sub> (CZTS) is a promising sustainable photovoltaic material and colloidal dispersions of wurtzite or kesterite CZTS nanocrystals are often used to make thin polycrystalline films for solar cells. This requires control of the nanocrystal phases *via* the synthesis. We studied the microwave-assisted solvothermal synthesis of CZTS nanocrystals from metal salts and thiourea in ethylene glycol in the presence of various excess sulfur sources. Relative fractions of the kesterite and wurtzite phases depend on the excess sulfur source, the oxidation state of Sn, and the sulfur-to-total-metal -cation (S : M) ratio used in the synthesis. When the excess sulfur source contains an amino group, a Zn–Sn intermediate forms and allows the CZTS phase to be varied between kesterite and wurtzite *via* the Sn initial oxidation state and S : M ratio. When the excess sulfur source contains an amino group, synthesis using Sn(II) salts and low S : M (1.9) favors the formation of the wurtzite phase, whereas synthesis using high S : M ratio (>4) favors the formation of the kesterite phase. Only the kesterite phase is obtained when Sn(IV) reagent is used, regardless of S : M ratio. When the excess sulfur source does not have an amino group, only the wurtzite phase is obtained under the conditions studied, regardless of the oxidation state of the Sn precursor or the S : M ratio; in these cases, the Zn–Sn intermediate does not form and the precursor to wurtzite appears to be copper sulfide.

Received 13th July 2017  
Accepted 18th October 2017

DOI: 10.1039/c7ta06086f

rsc.li/materials-a

## Introduction

Thin film solar cells based on direct band gap semiconductors such as Cu(In,Ga)Se<sub>2</sub> (CIGS) and CdTe require a hundred times less absorber material than silicon solar cells and are therefore expected to be less expensive.<sup>1,2</sup> Solar cells based on CIGS have already reached efficiencies as high as 21.7%, comparable to silicon solar cells.<sup>3</sup> However, CIGS-based solar cells are difficult to implement in large scale because indium is scarce and high in demand as an element in transparent conductive oxides used widely in the display industry.<sup>4</sup> A potential substitute for CIGS in

thin film solar cells is Cu<sub>2</sub>ZnSnS<sub>4</sub> (CZTS). CZTS is a p-type semiconductor with a band gap of 1.5 eV and high absorption coefficient (>10<sup>4</sup> cm<sup>-1</sup>) so that a few micrometer thick film absorbs nearly all photons with energies greater than the band gap. Moreover, CZTS is comprised of abundant and non-toxic elements,<sup>5–7</sup> and CZTS-based solar cell efficiencies have already reached 12.7%.<sup>8</sup>

CZTS can crystallize in kesterite, stannite, primitive mixed Cu–Au (PMCA), and wurtzite crystal structures.<sup>9</sup> Besides these, other structures derived from wurtzite do also form, such as wurtzite-derived monoclinic, and wurtzite-derived orthorhombic, which are also known as wurtzite–kesterite and wurtzite–stannite phases, respectively.<sup>10,11</sup> The thermodynamically stable crystalline phase of CZTS is tetragonal kesterite (space group  $\bar{I}4$ ), whereas wurtzite ( $P6_3mc$ ) is considered to be metastable.<sup>10</sup> Because the kesterite and stannite phases differ only in the ordering of the Cu<sup>+</sup> and Zn<sup>2+</sup> cations, routinely used characterization methods such as X-ray diffraction and Raman spectroscopy cannot distinguish between these two phases regardless of the underlying lattice (tetragonal or hexagonal, *i.e.*, wurtzite). Perhaps the only characterization technique that can possibly distinguish between kesterite and stannite phases is neutron diffraction. Indeed, using neutron diffraction Schorr *et al.*<sup>12</sup> have shown that tetragonal kesterite forms when the synthesis is carried out in a way to favor the equilibrium phase. However, Schorr *et al.* also showed that there could still be Cu<sup>+</sup>

<sup>a</sup>Department of Chemistry, University of Minnesota, Smith Hall, 207 Pleasant Street SE, Minneapolis, MN 55455, USA. E-mail: apinto2@ithaca.edu; rleepenn@umn.edu

<sup>b</sup>Department of Chemical Engineering and Materials Science, University of Minnesota, Amundson Hall, 421 Washington Ave. SE, Minneapolis, MN 55455-0132, USA. E-mail: aydil@umn.edu

† Electronic supplementary information (ESI) available: Rietveld refinement procedure, crystal size estimates, elemental mapping using STEM-HAADF, X-ray diffraction patterns, additional synthesis experiments and characterization. See DOI: 10.1039/c7ta06086f

‡ Present address: Department of Chemistry, Ithaca College, Center for Natural Sciences, 953 Danby Road, Ithaca, NY 14850, USA.

§ Present address: Department of Physics and Astronomy and Wright Center for Photovoltaic Innovation and Commercialization, University of Toledo, Toledo, OH, 43606, USA.

¶ Present address: Department of Chemistry, Brown University 324 Brooks St, Providence, RI 02912, USA.

and  $\text{Zn}^{2+}$  cation disorder in the product. The analogous study to distinguish between wurtzite–kesterite and wurtzite–stannite was recommended by Regulacio *et al.*<sup>13</sup> but to our knowledge has not been carried out yet. In this manuscript, we refer to the tetragonal phase as kesterite. We refer to the wurtzite phase without any qualification on whether it is kesterite–wurtzite or stannite–wurtzite because we cannot tell the difference without conducting neutron diffraction on nearly phase pure samples. Of course, cation disorder can also be present but is also difficult to quantify.

In 2011, Lu *et al.*<sup>14</sup> synthesized the metastable wurtzite phase of CZTS by injecting metal chloride solutions in dodecanethiol into a hot mixture of dodecanethiol, oleylamine, and oleic acid. They hypothesized that dodecanethiol played an important role in obtaining the metastable wurtzite phase. Indeed, most methods for synthesizing wurtzite CZTS employ a surfactant such as hexadecanethiol, dodecanethiol, oleylamine, and trioctylamine during synthesis.<sup>15,16</sup> Regulacio *et al.*<sup>13</sup> showed that, in one mechanism, the role of the surfactant is to stabilize intermediate products that help the formation of wurtzite CZTS while restricting the formation of the tetragonal phase. Regulacio *et al.*<sup>13</sup> also found that wurtzite CZTS formation was favored when long chain alkanethiols helped nucleation and growth of hexagonal  $\text{Cu}_{1.94}\text{S}$  nanocrystals, which in turn allowed wurtzite CZTS to template on these  $\text{Cu}_{1.94}\text{S}$  nanocrystals. The heterostructured wurtzite–CZTS– $\text{Cu}_{1.94}\text{S}$  nanocrystals eventually converted to wurtzite CZTS *via* cation diffusion.<sup>13</sup> Thus, the surfactants appear to stabilize a copper sulfide intermediate that locks in the crystal structure.

Another approach to synthesize wurtzite CZTS phase is *via* cation substitution into a wurtzite intermediate. For instance, Wang and co-workers prepared wurtzite CZTS by diffusing Zn into wurtzite  $\text{Cu}_2\text{SnS}_3$  and replacing half the copper cations with Zn.<sup>17</sup> This idea is related to that used by Regulacio because it allows the system to choose the final crystal structure through an intermediate nanocrystal with hexagonal symmetry. Li *et al.*<sup>18</sup> varied the phase composition of their product from wurtzite to kesterite CZTS by varying the sulfur sources mixed into oleylamine. Using elemental sulfur dissolved in oleylamine produced kesterite CZTS *via* a rapid reaction, whereas moderating the reaction rate by using dodecanethiol allowed the formation of a copper sulfide intermediate ( $\text{Cu}_7\text{S}_4$ ) and produced wurtzite CZTS. Lin *et al.*<sup>19</sup> used a microwave solvothermal method and varied the volume fraction of ethylenediamine and water as solvents. When only ethylenediamine was used, they obtained wurtzite CZTS whereas a 50–50% mixture of ethylenediamine and water lead to kesterite CZTS. Again, wurtzite formation was preceded by the formation of a sulfide, this time  $\text{Cu}_2\text{S}$ , as the intermediate.

Thus, the work to date shows that wurtzite is obtained when the reaction is slowed and copper sulfide intermediates are allowed to form though not all the copper sulfide intermediates identified by various groups were the same. The reaction rate and the formation of the intermediate could be controlled by varying the capping ligands, sulfur source, or the solvent. Although, there have been numerous studies that showed the synthesis of wurtzite nanocrystals, mechanisms of their

production and the factors that control the phase composition remain unclear in many cases.<sup>20–24</sup>

One approach to making thin polycrystalline kesterite CZTS films for solar cells is to anneal coatings cast from nanocrystal dispersions in sulfur or selenium vapour.<sup>25–28</sup> During annealing the microstructure of the coatings cast from wurtzite or kesterite nanocrystals evolve differently.<sup>29</sup> For example, grain growth is faster, begins at lower temperature, and is more facile when metastable wurtzite nanocrystals are transformed into kesterite grains. This motivates the search for controlled synthetic routes that are able to selectively give one crystalline phase (*e.g.*, wurtzite) over the other (*e.g.*, kesterite).<sup>29,30</sup>

Herein, we studied several factors that play a key role in the control of the CZTS phase from wurtzite to kesterite. These factors include the sulfur source, molar ratio of sulfur to total metal ions, and the initial oxidation state of the Sn reagent. Surfactant or capping agents were not used in any of the syntheses. There are multiple paths to the metastable wurtzite phase. Instead of the copper sulfides that appeared to be the key intermediate in previous work, we show that the intermediate that leads to the wurtzite phase in our work is a Zn–Sn intermediate complex, whose formation is controlled by the oxidation state of Sn and the presence of an amino group in the sulfur source. The absence of surfactants is also a significant advantage of our method, since long chain organic ligands are difficult to remove from particle surfaces after synthesis, and can hinder charge transport in films prepared from these particles.<sup>31</sup> Additionally, the microwave based solvothermal approach described here is reproducible, fast, and scalable. In a typical synthesis significant amounts (0.4 g) of CZTS particles can be synthesized in just 20 minutes.

## Experimental

### Materials

Copper(II) acetate monohydrate ( $\text{CuAc}_2 \cdot \text{H}_2\text{O}$  ACS reagent, >98% Sigma-Aldrich), copper(I) acetate ( $\text{CuAc}$  97% Sigma Aldrich), zinc acetate dihydrate ( $\text{ZnAc}_2 \cdot 2\text{H}_2\text{O}$  ACS reagent Acros Organic), tin(II) chloride ( $\text{SnCl}_2$  98% Sigma Aldrich), tin(IV) chloride pentahydrate ( $\text{SnCl}_4 \cdot 5\text{H}_2\text{O}$  Sigma Aldrich), thiourea ( $\text{CH}_4\text{N}_2\text{S} \geq 99.0\%$  Sigma Aldrich), L-cysteine ( $\text{C}_3\text{H}_7\text{NO}_2\text{S}$  97% Sigma Aldrich), thioglycolic acid ( $\text{C}_2\text{H}_4\text{O}_2\text{S}$  98% Sigma Aldrich), 3-mercaptopropionic acid ( $\text{C}_3\text{H}_6\text{O}_2\text{S} \geq 99.0\%$  Sigma Aldrich) ethylene glycol (Fisher Scientific), methanol (Sigma Aldrich), and ethanol (Decon – 200 Proof) were used as received and without additional purification.

### CZTS nanoparticles synthesis

In a typical synthesis,  $1.7 \times 10^{-3}$  mol of  $\text{CuAc}_2 \cdot \text{H}_2\text{O}$ ,  $1.0 \times 10^{-3}$  mol of  $\text{ZnAc}_2 \cdot 2\text{H}_2\text{O}$ , and  $1.0 \times 10^{-3}$  mol of  $\text{SnCl}_2$  were added to 30 mL ethylene glycol with stirring. Variable amounts of thiourea were added to achieve a sulfur to total (Cu, Zn and Sn) metal ion molar ratio (S : M) between 1 and 6.2, *i.e.*,  $S : M = n_{\text{S}} / (n_{\text{Cu}} + n_{\text{Zn}} + n_{\text{Sn}})$ , where  $n_i$  is the number of moles of species *i*. After sonicating for 30 minutes, this reaction mixture was sealed in a Teflon vial, which was placed inside a SiC sleeve and

loaded into an Anton Parr Multiwave Pro microwave. The reaction mixture was heated from room temperature to 160 °C in 15 minutes, using 300 W of power. Following this temperature ramp, the reaction mixture was maintained at 160 °C for 5 minutes. After 5 minutes, the power was turned off, and the reaction mixture was cooled to 55 °C in 20 minutes *via* convective flow induced by the fans in the microwave. The microwave is equipped with a turntable, which spins the vial at 2 rpm during the entire procedure. Magnetic stirring was not used during the synthesis. The reaction mixture temperature was measured using an infrared sensor.

After cooling, the contents of the Teflon vial were transferred to a centrifuge tube and centrifuged at 8500 rpm (8450 rcf) for 15 minutes. The supernatant was discarded, ethanol was added, and the resulting dispersion in ethanol was centrifuged at 8450 rcf for 5 minutes. This centrifugation–redispersion cycle was repeated four times. Finally, the precipitate was dispersed in methanol. The effect of the excess sulfur sources other than thiourea was studied by adding appropriate moles (to achieve a particular S : M ratio) of *L*-cysteine, thioglycolic acid or 3-mercaptopropionic acid to the mixture of CuAc<sub>2</sub>·H<sub>2</sub>O ( $1.7 \times 10^{-3}$  mol), ZnAc<sub>2</sub>·2H<sub>2</sub>O ( $1.0 \times 10^{-3}$  mol), SnCl<sub>2</sub> ( $1.0 \times 10^{-3}$  mol), and thiourea ( $4.0 \times 10^{-3}$  mol) in 30 mL ethylene glycol.

### Experiments varying the synthesis temperature

To study the effect of temperature, the microwave heating was stopped during the ramp at different temperatures. For instance, a reported synthesis temperature of 75 °C means that the microwave heating was turned off when the temperature reached 75 °C; after the microwave heating was turned off, the reaction mixture immediately started to cool.

### Experiments varying the copper and tin oxidation states

In addition to the synthesis with CuAc<sub>2</sub>·H<sub>2</sub>O and SnCl<sub>2</sub>, the following combinations of copper and tin reagents were also used: CuAc and SnCl<sub>2</sub>, CuAc and SnCl<sub>4</sub>·5H<sub>2</sub>O; and CuAc<sub>2</sub>·H<sub>2</sub>O and SnCl<sub>4</sub>·5H<sub>2</sub>O. In all these experiments,  $1.7 \times 10^{-3}$  mol of the copper reagent,  $1.0 \times 10^{-3}$  mol of ZnAc<sub>2</sub>·2H<sub>2</sub>O, and  $1.0 \times 10^{-3}$  mol of the tin reagent were used. Thiourea was added in the appropriate amounts to vary the S : M ratios between 1.9 and 6.2. The ultrasonication and microwave heating procedures were the same as used in the synthesis with CuAc<sub>2</sub>·H<sub>2</sub>O and SnCl<sub>2</sub>.

### Product labelling convention

Because of the large number of synthesis variables, we use a convenient product-labelling scheme. The synthesis products are labeled as Cu(N)<sub>x</sub>Sn(L)<sub>y</sub>XCS<sub>S</sub>:M<sub>T</sub>, where N and L represent copper and tin oxidation states, respectively; XCS represents the source of sulfur excess, where Tu, Cyst, TGacid and MCPacid stand for thiourea, *L*-cysteine, thioglycolic acid, and 3-mercaptopropionic acid, respectively. S : M is the sulfur-to-total-metal-cation ratio; and T is the maximum temperature reached during the microwave heating.

### Characterization

Products were characterized using X-Ray Diffraction (XRD), Raman scattering, optical and infrared spectroscopy, and various electron microscopies. Specifically, XRD patterns from the products were collected using a Pananalytical X'Pert Pro X-ray diffractometer (Co K $\alpha$  radiation with a wavelength of 1.7890 Å) equipped with a X'Celerator detector. The XRD patterns were collected from 16 to 85° (2 $\theta$ ), with an effective step size of 0.0167° and 50 s dwell time per step. The crystalline phase percentage was estimated using Rietveld refinement, with the details provided in the ESI.†

Raman spectra were collected from dried powders using a Witec Confocal micro-Raman spectrometer with a green 532 nm laser as the excitation source. The laser power was fixed at 1 mW, and each spectrum was integrated over 150 seconds. Optical absorption spectra were collected from diluted methanol dispersions of the nanocrystals, using an Agilent 8453 spectrophotometer. For infrared spectroscopy analyses, nanocrystals were drop cast from methanol dispersions onto NaCl windows, which were then dried in air. Infrared spectra were collected using a Nicolet Series II Magna-IR System 750 FTIR in the transmittance mode. For elemental analysis using Inductively Coupled Plasma Optical Emission Spectrometry (ICP-OES), 20  $\mu$ L of supernatant were dissolved in 50 mL of H<sub>2</sub>O and injected in a iCap 7600 Duo ICP-OES Analyzer.

For SEM analyses, the nanocrystals dispersed in methanol were sonicated for 15 minutes, drop cast onto silicon substrates, and dried in air. The dried nanocrystals were then examined in a JEOL 6500 SEM, at an acceleration voltage of 5 kV. Elemental composition of the nanocrystals was determined using Energy Dispersive X-ray Spectroscopy (EDS) using a Thermo-Noran Vantage system equipped with an EDS detector coupled to the JEOL 6500 SEM. The acceleration voltage was adjusted to 15 kV for all EDS measurements, the EDS spectra were collected in the standardless mode, with the ratio of the elements calculated based on the reference spectra provided by the software System SIX. For each sample, the elemental compositions were determined at ten different locations and these values were averaged.

Samples for TEM characterization were prepared by drop casting nanocrystals onto Cu TEM grids (SPI 200 mesh holey carbon coated) from methanol dispersions after sonicating for at least 30 minutes. The nanocrystals were imaged using a FEI T12 microscope, with acceleration voltage of 120 kV. High-resolution images were collected using a FEI Tecnai G2 F-30, with acceleration voltage of 300 kV. Selected area electron diffraction patterns were collected using this same microscope. Scanning transmission electron microscopy (STEM) was performed using an FEI Tecnai G2 field-emission S/TEM operating at an accelerating voltage of 80 kV. High-angle annular dark field (HAADF) images were collected using an E. A. Fischione annular detector. Energy-dispersive X-ray spectroscopy (EDS) spectra were collected using the ChemiSTEM EDX spectrometer. EDS maps were collected while rastering the beam over the sample, which facilitated

minimization of beam damage. A probe current of  $\sim 0.1$  nA was used, and maps were collected over a minimum of five minutes. Data were analyzed using ESPRIT software (version 1.9.4).

## Results and discussion

### Effect of S : M ratio on the phase of the nanocrystals synthesized using Cu(II) and Sn(II) reagents

When Cu(II) and Sn(II) precursors were used and the sole sulfur source was thiourea, the kesterite-to-wurtzite ratio in the synthesis product could be changed by varying the S : M ratio. Fig. 1a shows the XRD patterns from nanocrystals synthesized using Cu(II) and Sn(II) reagents and thiourea as the sole sulfur source while varying the S : M ratio. The stoichiometric reaction mixture (S : M = 1) results in the formation of impurity phases such as  $\text{Cu}_3\text{SnS}_4$ ,  $\text{Cu}_4\text{SnS}_4$ , and elemental sulfur. The kesterite-to-wurtzite ratio

increases with increasing S : M ratio (Fig. 1b). The nanocrystal product is comprised of approximately 50% wurtzite and 50% kesterite for S : M between 2 and 4. When S : M is greater than 4, the kesterite fraction rises to 80% (see ESI Table S2† for details).

The nanocrystal size estimated using Scherrer equation, for the peak located at  $2\theta$  around  $32^\circ$ , corresponding to the (112) planes of the wurtzite phase, and (002) planes of the kesterite phase, varied between 6.4 and 3.7 nm and decreased with increasing S : M. The product containing mostly kesterite had the smallest average crystallite size (ESI Table S3†).

Raman spectra (Fig. 2) are consistent with the XRD results and exhibit a high intensity peak at  $328\text{ cm}^{-1}$  for all products prepared with a S : M of 1.9 or greater. The most intense Raman peak from CZTS is expected around  $336\text{--}339\text{ cm}^{-1}$ .<sup>32,33</sup> However, it is common to observe this peak shifted to lower wavenumbers (e.g.,  $328\text{--}331\text{ cm}^{-1}$ ). This peak shift is thought to be due to inhomogeneity within the disordered cation sublattice.<sup>34,35</sup> Peaks related to secondary phases such as  $\text{Cu}_2\text{S}$ ,  $\text{SnS}$ ,  $\text{SnS}_2$ ,  $\text{ZnS}$ ,  $\text{Cu}_2\text{SnS}_3$ , and  $\text{Cu}_3\text{SnS}_4$  were not detected, though some of these compounds ( $\text{ZnS}$ ,  $\text{Cu}_2\text{SnS}_3$ , and  $\text{Cu}_3\text{SnS}_4$ ) have partially overlapping peaks with CZTS and presence of amounts undetectable via XRD and Raman can not be ruled out.<sup>33</sup>

Bright field TEM images of the Cu(II)\_Sn(II)\_Tu\_1.9\_160 °C nanocrystals (Fig. 3a) revealed the presence of two types of nanocrystal shapes. Some nanocrystals were anisotropic and oblate while others were more spheroidal (see also Fig. S1 in ESI†). Anisotropic oblate nanocrystal shapes have been observed previously when wurtzite CZTS was present.<sup>36</sup> The observation of two types of morphology is consistent with the XRD results, which demonstrate that the product is a mixture of kesterite and wurtzite CZTS: we associate the oblate morphology with wurtzite CZTS and the spheroid morphology with kesterite CZTS. The SAED patterns (Fig. 3b and e) exhibit rings with  $d$ -spacings that are consistent with both the wurtzite and the kesterite phases. The SAED pattern (Fig. 3b) is consistent with the XRD results, showing more intense reflections

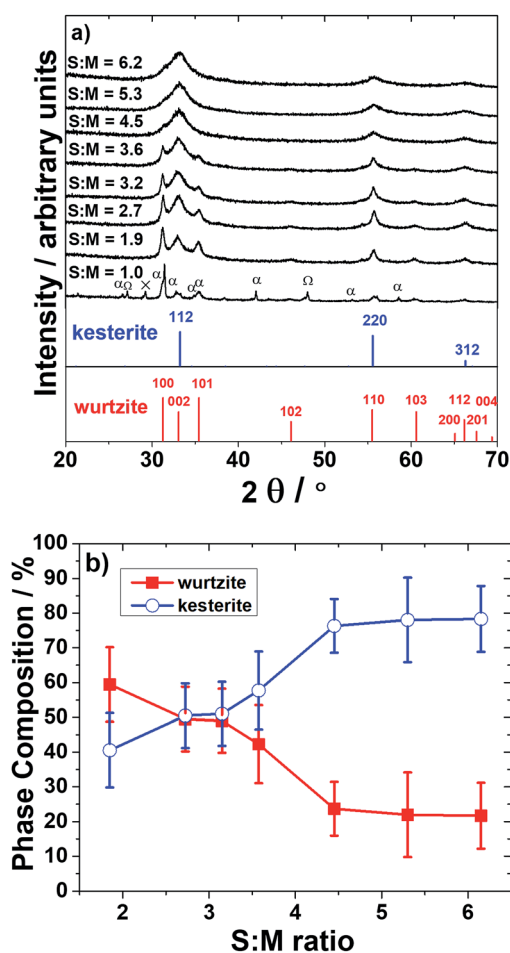


Fig. 1 (a) XRD patterns from nanocrystals synthesized using  $\text{Cu}^{2+}$ , and  $\text{Sn}^{2+}$  at  $160^\circ\text{C}$  using different S : M ratios. The sulfur source was thiourea (i.e.,  $\text{Cu(II)}_{\text{Sn(II)}}\text{Tu}_S\text{:M}_{160^\circ\text{C}}$  where S : M was varied between 1.0 and 6.2). XRD patterns for wurtzite (simulated) and kesterite (PDF# 00-0026-0575) CZTS are shown at the bottom. Peaks labeled as  $\Omega$  are consistent with  $\text{Cu}_3\text{SnS}_4$  (PDF 00-036-0218),  $\alpha$  with  $\text{Cu}_4\text{SnS}_4$  (PDF 00-029-0584), and  $\times$  with elemental sulfur (PDF 00-008-0247) (b) phase composition estimated from Rietveld refinement analysis of the XRD patterns shown in (a). Error bars were determined from triplicate analyses, as described in the ESI.†

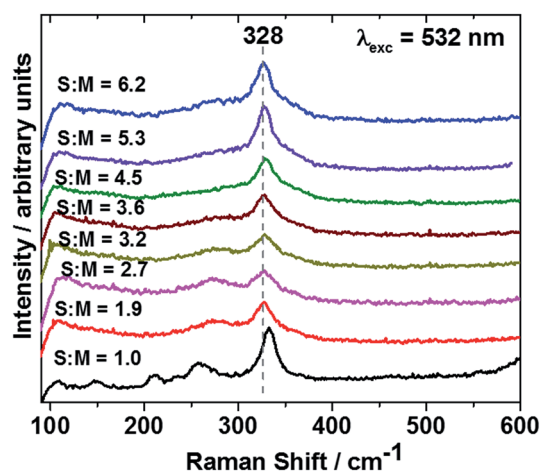


Fig. 2 Raman spectra of the nanocrystals synthesized from  $\text{Cu}^{2+}$ , and  $\text{Sn}^{2+}$  at  $160^\circ\text{C}$ , while varying the S : M ratio. The sulfur source was thiourea: (i.e.,  $\text{Cu(II)}_{\text{Sn(II)}}\text{Tu}_S\text{:M}_{160^\circ\text{C}}$  where S : M was varied between 1.0 and 6.2).

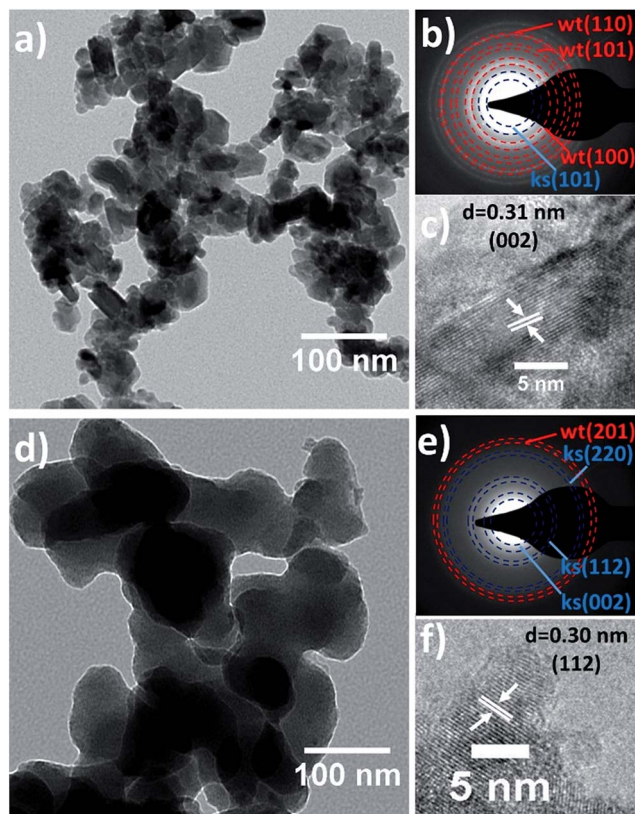


Fig. 3 (a) TEM, (b) SAED (c) HR-TEM images of the Cu(II)<sub>1</sub>Sn(II)<sub>1.9</sub>Tu<sub>160</sub> °C and (d) TEM, (e) SAED (f) HR-TEM of the Cu(II)<sub>1</sub>Sn(II)<sub>6.2</sub>Tu<sub>160</sub> °C nanocrystals.

related to the wurtzite phase than for kesterite phase. High-resolution images from an oblate nanocrystal show lattice fringes with spacing consistent with the (002) of wurtzite CZTS (Fig. 3c). This would be consistent with our association of the oblate anisotropic nanocrystals with the wurtzite phase. In contrast, in the TEM image of Cu(II)<sub>1</sub>Sn(II)<sub>6.2</sub>Tu<sub>160</sub> °C (Fig. 3f), the nanocrystals appear spheroidal in shape, and the reflections consistent with the kesterite phase are substantially more intense, which is consistent with the XRD results. The spheroid nanocrystals showed lattice fringes with spacings that match the (112) *d*-spacing of kesterite (Fig. 3f). The Cu(II)<sub>1</sub>Sn(II)<sub>1.9</sub>Tu<sub>160</sub> °C and Cu(II)<sub>1</sub>Sn(II)<sub>6.2</sub>Tu<sub>160</sub> °C samples were analyzed using HAADF-STEM. The STEM-EDS maps revealed that Cu, Zn, Sn and S are homogeneously distributed in both samples (Fig. S2 in ESI<sup>†</sup>).

#### Effect of Cu and Sn initial oxidation states

Varying the oxidation states of the Sn and Cu precursors led to the conclusion that the initial tin oxidation state is an important parameter and is one of the factors in the synthesis that determines the crystalline phase of the product. To support this conclusion Fig. 4 shows the XRD patterns from nanocrystals synthesized using different pairings of Cu(I) and Cu(II) reagents with Sn(II) and Sn(IV) reagents while holding S : M constant at 1.9 or 6.2: the excess sulfur was provided using thiourea. The

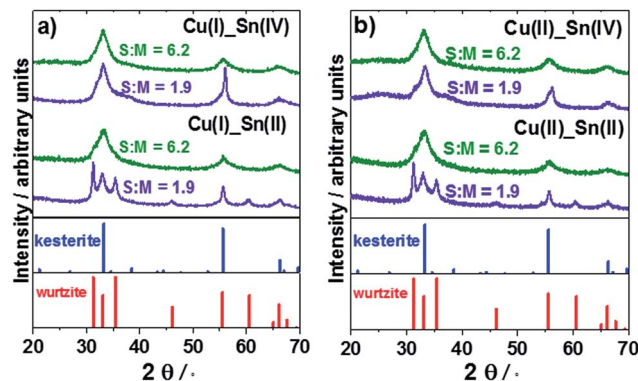


Fig. 4 XRD patterns for (a) Cu(I)<sub>1</sub>Sn(IV)<sub>1</sub>Tu<sub>S</sub> : M<sub>160</sub> °C (bottom), and Cu(I)<sub>1</sub>Sn(IV)<sub>1</sub>Tu<sub>S</sub> : M<sub>160</sub> °C (top) (b) Cu(II)<sub>1</sub>Sn(II)<sub>1</sub>Tu<sub>S</sub> : M<sub>160</sub> °C (bottom), and Cu(II)<sub>1</sub>Sn(IV)<sub>1</sub>Tu<sub>S</sub> : M<sub>160</sub> °C (top).

nanocrystal compositions are in ESI Table S4.<sup>†</sup> When the S : M is 6.2, the majority phase is always kesterite, regardless of the oxidation states of Sn and Cu. However, when the S : M is 1.9, the dominant product is wurtzite when Sn(II) is used and kesterite when Sn(IV) is used, regardless of the copper oxidation state.

#### Effect of excess sulfur source

We also studied the effect of changing the excess sulfur source by substituting *L*-cysteine, thioglycolic acid or 3-mercaptopropionic acid for excess thiourea. We conducted experiments where we varied the excess sulfur source, Sn oxidation state (Sn(II) or Sn(IV)), and S : M ratio, S : M = 1.9 or 3.6. Fig. 5 shows the XRD patterns from the products of these experiments. There are two noticeable trends with the source of sulfur excess. First, the molecules containing an amino group (NH<sub>2</sub>), *e.g.*, thiourea and *L*-cysteine, produce mostly kesterite CZTS when Sn(IV) is used as tin source but tend to produce wurtzite when Sn(II) is used. On the other hand, molecules without NH<sub>2</sub> groups, like thioglycolic acid and 3-mercaptopropionic acid, when used as source of excess sulfur always produce wurtzite CZTS, regardless of the initial tin oxidation state.

#### On the mechanism and precursors to CZTS formation

Table 1 summarizes the dominant phases obtained with different excess sulfur sources, tin sources and S : M ratios. Thiourea was always necessary in at least stoichiometric amounts to form CZTS. Use of other sulfur sources without thiourea did not produce CZTS (see ESI Fig. S3<sup>†</sup>). While there are combinations of synthesis variables that lead to predominantly wurtzite or kesterite phases, there does not appear to be neat and obvious trends, perhaps with the exception of the trend with amino groups: it appears that presence of the amino group in the excess sulfur source differentiates the Sn(II) and Sn(IV) sources. Infrared spectra of the surfaces of these nanocrystals were consistent with the presence of ethylene glycol (ESI Fig. S4<sup>†</sup>). The explanation of Table 1 requires experiments aimed at revealing the formation mechanisms. Towards this end we conducted experiments at lower temperatures in

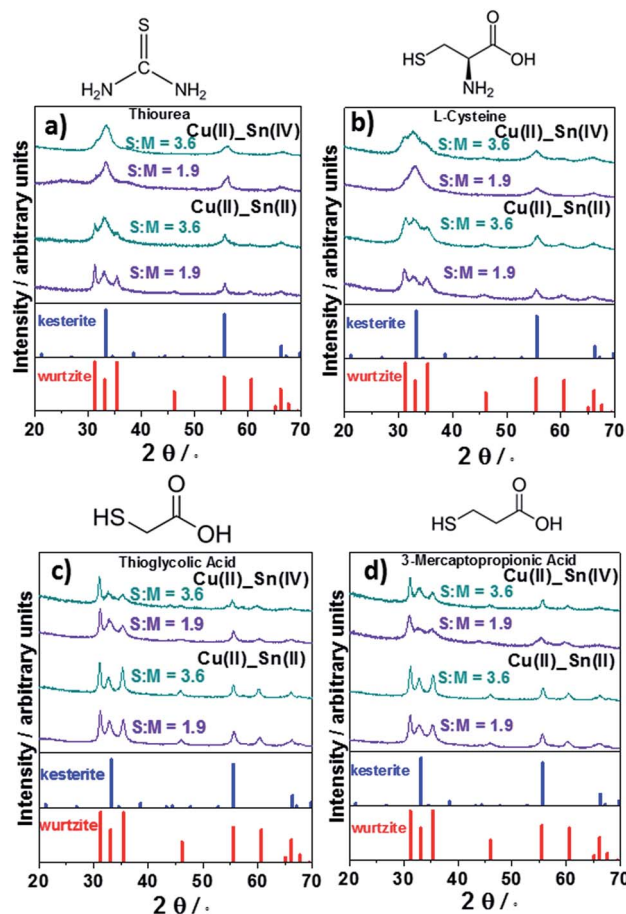


Fig. 5 XRD patterns of the CZTS nanocrystals synthesized using different excess sulfur sources, Sn oxidation states, and S : M = 1.9 or 3.6. Sulfur excess sources were (a) thiourea, (b) L-cysteine, (c) thioglycolic acid, (d) 3-mercaptopropionic acid (see also Table S5† for wurtzite and kesterite fractions calculated via Rietveld refinement).

attempts to slow the formation of the CZTS nanocrystals and observe any reaction intermediates.

Considering the possibility that the preferential synthesis of one phase over another may be related to the differences in their formation mechanisms we explored the synthesis at temperatures lower than 160 °C. Fig. 6a shows the XRD patterns from products synthesized at various temperatures between 25 °C and 160 °C for S : M = 1.9 with Sn(II) source and thiourea,

Table 1 Summary of the dominant phases formed using different combinations of tin and excess sulfur sources and with low and high S : M ratios. TGAcid is thioglycolic acid and MPAcid is 3-mercaptopropionic acid

Excess S	Low S : M		High S : M	
	Sn(II)	Sn(IV)	Sn(II)	Sn(IV)
Thiourea	W	K	K	K
L-Cysteine	W	K	W	K
TGacid	W	W	W	W
MPacid	W	W	W	W

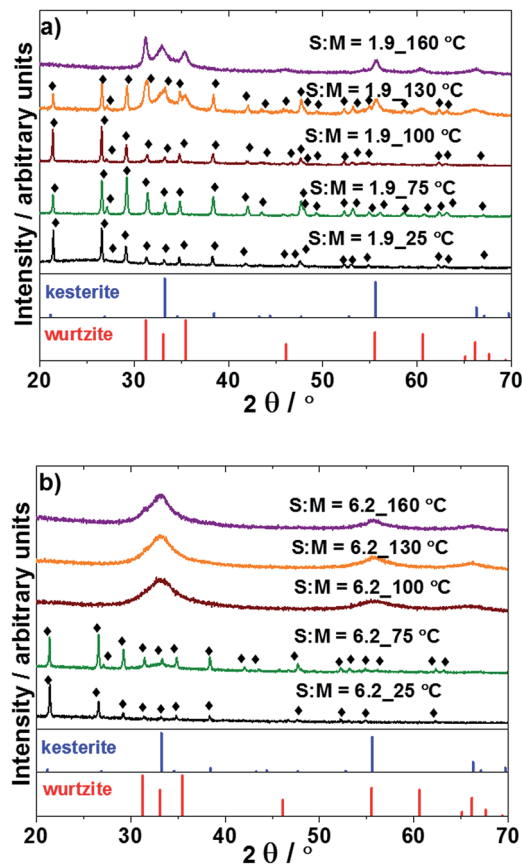


Fig. 6 XRD pattern from the nanocrystals synthesized at different temperatures,  $T$  from Sn(II) source: (a) Cu(II)\_Sn(II)\_Tu\_1.9\_ $T$ , (b) Cu(II)\_Sn(II)\_Tu\_6.2\_ $T$ ; ◆ denotes the diffraction from the Zn–Sn intermediate.

conditions that favor the formation of the wurtzite phase. At and below 100 °C, we find multiple diffraction peaks. The reaction of the Zn and Sn(II) in ethylene glycol yields a product with 1 : 1 Zn : Sn ratio, with XRD peaks identified with black diamonds in Fig. 6 (see also Fig. S5 and S6 in ESI†), corresponding to Zn–Sn intermediates, as discussed by Wang,<sup>37</sup> Ng,<sup>38</sup> and Das.<sup>39</sup> The XRD peaks for the wurtzite CZTS begin to appear at 130 °C. Zn–Sn intermediate intermediates are the only products below 100 °C. It is well known that Zinc(II) acetate can react with thiourea to form the bithiourea zinc acetate complex ( $\text{Zn}((\text{NH}_2\text{CSNH}_2)_2(\text{CH}_3\text{COO})_2)$ ).<sup>40,41</sup> It is also known that  $\text{SnCl}_2$  can form complexes with thiourea. For instance, when  $\text{Sn}^{2+}$  and thiourea are mixed in 1 : 1 mole ratio, they form thioureatin(II) chloride ( $\text{Sn}(\text{NH}_2\text{CSNH}_2)_2\text{Cl}_2$ ), and when the Sn : thiourea ratio is between 1 : 2 and 1 : 6, the pentathioureadi-[tin(II)chloride] dihydrate ( $\text{Sn}_2(\text{NH}_2\text{CSNH}_2)_5\text{Cl}_4 \cdot 2\text{H}_2\text{O}$ ) complex.<sup>42</sup> Thus, the formation of a Zn–Sn complex is not surprising. Unfortunately, we have been unable to grow large single crystals of this Zn–Sn intermediate to conduct X-ray diffraction, which leaves us unable to assign a definite formula and structure. However, after a thorough search on Cambridge Structural Database (CSD), we found that the XRD pattern of this Zn–Sn intermediate resembles a pattern formed by a mixture of thioureatin(II) chloride (CSD code: CAPWEV)<sup>43</sup> and a zinc succinate thiourea

complex called catena-((m2-Succinato-O,O')-bis(thiourea-S)-zinc) (CSD code: FELXEA).<sup>44</sup> Based on the similarity between the XRD pattern of this zinc succinate thiourea complex and the Zn–Sn intermediate, one possibility is that the intermediate is a mixture of the thioureatin(II) chloride complex and another complex that contains intermediate and thiourea ligands.<sup>44</sup> Further information about the XRD patterns of the thioureatin(II) chloride and catena-((m2-Succinato-O,O')-bis(thiourea-S)-zinc) can be found in the ESI (Fig. S5, the additional data in Fig. S6–S9 and the accompanying discussion).<sup>†</sup> Another possibility is that the Zn–Sn intermediate may be a bi-nuclear complex containing Zn and Sn. A Zn–Sn intermediate is also formed when L-cysteine is used as the excess sulfur source but not with other sulfur sources such as TGAcid and MPAcid, implicating the amino group in the formation of this complex intermediate. Another possibility is that the Zn–Sn intermediate could be a compound with the formula similar to  $\{[\text{Zn}(\text{amine containing ligand})_x]_2[\text{Sn}_2\text{S}_6]\}_n$ . Similar compounds containing Ni instead of Zn with this structure have already been synthesized at room temperature and reported in the literature.<sup>45</sup> Importantly, the Zn–Sn intermediate obtained at 25 °C did not contain any copper. Copper begins to incorporate as the temperature is raised (Fig. S6<sup>†</sup>). Analysis of the supernatant from the reaction that produces solid Zn–Sn intermediate at 25 °C using ICP-OES contained  $\approx 900$  times more Cu than Zn, indicating clearly that copper remains in solution, perhaps as an amino complex. The same analysis on the supernatant from the reaction at 90 °C contained  $\approx 20$  times more Cu than Zn, consistent with increased Cu incorporation into the solid as temperature is raised.

In contrast, when the synthesis is conducted using higher sulfur excess ( $S : M = 6.2$ ), Zn–Sn intermediates are observed only up to 75 °C, with CZTS peaks just beginning to appear at lower temperature. However, these CZTS peaks are those expected from the kesterite phase and not the wurtzite phase. For  $S : M = 6.2$  at and above 100 °C only the XRD peaks from kesterite CZTS are observed, with no evidence of wurtzite formation. The XRD data from the products synthesized with a high  $S : M$  ratio ( $S : M = 6.2$ ) show that the kesterite phase is formed directly, without the formation of the wurtzite phase. Similarly, the XRD data from the products synthesized with a low  $S : M$  ratio ( $S : M = 1.9$ ) show that the wurtzite phase is formed directly without the formation of the kesterite phase. In other words, there is no phase transition from wurtzite to kesterite or *vice versa* during synthesis. This indicates that the  $S : M$  ratio directly influences the nucleation and growth of CZTS, an issue that we will revisit shortly.

The same low temperature experiments conducted with the Sn(IV) precursor did not yield the Zn–Sn intermediate complex. Instead, the XRD and SEM-EDS data show that the room temperature synthesis starting with Cu(II) and Sn(IV) precursors resulted in the formation only of elemental sulfur, with no evidence for the presence of any Zn–Sn intermediates, regardless of the  $S : M$  ratio (ESI Fig. S9 and Table S6<sup>†</sup>). The fact that thiourea does not bind Sn(IV) can be explained based on Pearson's Hard and Soft Acid Base Theory (HSAB),<sup>46</sup> since thiourea is a soft base and thus more likely to bind to Sn(II) and Zn(II),

which are both borderline acids, than to Sn(IV), which is a hard acid. Consequently, thiourea remains in the solution and decomposes, producing elemental sulfur. At higher temperatures Cu(II) and Sn(IV) precursors always lead to the formation of the kesterite phase. This observation implicates Zn–Sn intermediate as the precursors in the formation of the wurtzite phase when thiourea is used as sulfur excess source. That the Zn–Sn intermediates also form with other amine containing sulfur sources such as L-cysteine and leads to wurtzite formation supports this conclusion.

Fig. 7 compares SEM images of the Zn–Sn intermediate products, specifically, Cu(II)<sub>1</sub>Sn(II)<sub>1</sub>Tu<sub>1.9</sub> 25 °C (Fig. 7a) and Cu(II)<sub>1</sub>Sn(II)<sub>1</sub>Tu<sub>6.2</sub> 25 °C (Fig. 7c) with SEM images of the CZTS nanocrystals produced with the same tin and sulfur sources at 160 °C, specifically, Cu(II)<sub>1</sub>Sn(II)<sub>1</sub>Tu<sub>1.9</sub> 160 °C (Fig. 7b) and Cu(II)<sub>1</sub>Sn(II)<sub>1</sub>Tu<sub>6.2</sub> 160 °C (Fig. 7d). The morphologies of the Zn–Sn intermediate intermediates are sensitive to  $S : M$  ratio. When the  $S : M$  ratio employed is 1.9, the Zn–Sn intermediate particles are micron-sized hexagonal prisms (Fig. 7a), and the product formed after heating to 160 °C is wurtzite particles agglomerated into submicron spherules. In contrast an  $S : M$  ratio of 6.2 leads to the formation of hexagonal plates that have holes and this donut morphology is retained in the kesterite product that forms upon heating to 160 °C (Fig. 7c). The similarity between this morphology and those of CZTS nanocrystals (*e.g.*, Fig. 7d) is striking and immediately reinforces the conclusion that these Zn–Sn intermediate intermediates are precursors to CZTS formation. It thus seems that the hexagonal donuts transform to kesterite CZTS directly.

Even though the morphologies of the particles synthesized with  $S : M = 1.9$  and  $S : M = 6.2$  (*e.g.*, at 25 °C) are very different,

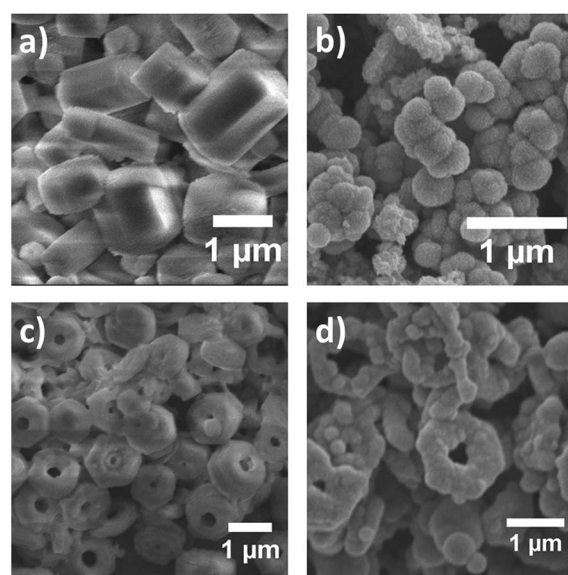


Fig. 7 SEM images of the nanocrystals (a) Cu(II)<sub>1</sub>Sn(II)<sub>1</sub>Tu<sub>1.9</sub> 25 °C, (b) Cu(II)<sub>1</sub>Sn(II)<sub>1</sub>Tu<sub>1.9</sub> 160 °C, (c) Cu(II)<sub>1</sub>Sn(II)<sub>1</sub>Tu<sub>6.2</sub> 25 °C, and (d) Cu(II)<sub>1</sub>Sn(II)<sub>1</sub>Tu<sub>6.2</sub> 160 °C. (a) and (c) are the Zn–Sn intermediate precursor nanocrystals whereas (b) and (d) are the CZTS nanocrystals formed from these precursors (see ESI Fig. S10<sup>†</sup> for additional SEM images).

their XRD patterns are nearly indistinguishable. These different precursor morphologies lead to the formation of wurtzite CZTS when  $S : M = 1.9$  and kesterite CZTS when  $S : M = 6.2$ . We believe that the morphologies of the Zn–Sn intermediate precursor mediate the rate of transformation to CZTS. We hypothesize that the formation of wurtzite CZTS is favored by slow conversion of the Zn–Sn intermediate precursor to CZTS *via* Cu diffusion. The hollow morphology presents a larger surface area facilitating faster diffusion of Cu into the intermediate and faster transformation, which favors the formation of the kesterite phase. In contrast, the transformation is slower with larger hexagonal prisms with less surface area, which slows the transport rate of Cu into the precursor particles favoring the slow formation of the wurtzite phase.

Table 1 also shows that wurtzite is always the major CZTS phase when thioglycolic acid or 3-mercaptopropionic acid are used as the excess sulfur source in the synthesis, regardless of the  $S : M$  ratio or the Sn oxidation state. This is in direct contrast to synthesis where amine containing excess sulfur sources are used where both the  $S : M$  ratio and the Sn oxidation state affects whether one obtains kesterite or wurtzite phases. We now show that the mechanism of the wurtzite CZTS formation when thioglycolic acid or 3-mercaptopropionic acid are used as the excess sulfur source is different than the mechanism discussed above where the precursor is a Zn–Sn intermediate. We further show that when thioglycolic acid or 3-mercaptopropionic acid are used the formation mechanism is similar to that previously revealed by Regulacio and others, and is *via* a copper sulfide intermediate as discussed in the Introduction.

Again, to reveal the intermediates we conducted the CZTS synthesis at temperatures lower than 160 °C, varying the Sn oxidation state. We changed the excess sulfur source to a molecule that does not have an amino group and cannot form the Zn–Sn intermediate precursor. Fig. 8 shows the XRD patterns from nanocrystals synthesized using thioglycolic acid as the excess sulfur source. Indeed, the Zn–Sn intermediate is not observed at any temperature. Instead, an amorphous powder is formed at temperatures lower than 75 °C. This amorphous powder begins to convert to crystalline  $Cu_{2-x}S$ , above 100 °C. We see clear diffraction peaks from  $Cu_{2-x}S$  (e.g., sample  $Cu(II)_{Sn(IV)}TGacid_{1.9_{100}}$  °C in Fig. 8b) when the tin source is Sn(IV) and weaker and broader diffraction peaks when the tin source is Sn(II) (e.g., sample  $Cu(II)_{Sn(II)}TGacid_{1.9_{100}}$  °C in Fig. 8a). We thus conclude that when the excess sulfur source does not have an amino group, the synthesis of the wurtzite CZTS phase proceeds through an  $Cu_{2-x}S$  intermediate. The presence of  $Cu_{2-x}S$  as intermediate leading to the formation of wurtzite CZTS and  $CuInS_2$  was previously observed and reported in the literature.<sup>20,47</sup>

While the amino group is necessary for the formation of the Zn–Sn intermediate, its precise role is not clear. One possibility is that the amino group is a part of the Zn–Sn intermediate. Alternatively, and perhaps more likely, the amino group complexes with copper present in solution, forming soluble copper–amino complexes leading to the formation of a copper-free Zn–Sn intermediate. Sequestration of copper in the soluble complex is also consistent with no  $Cu_{2-x}S$  intermediate

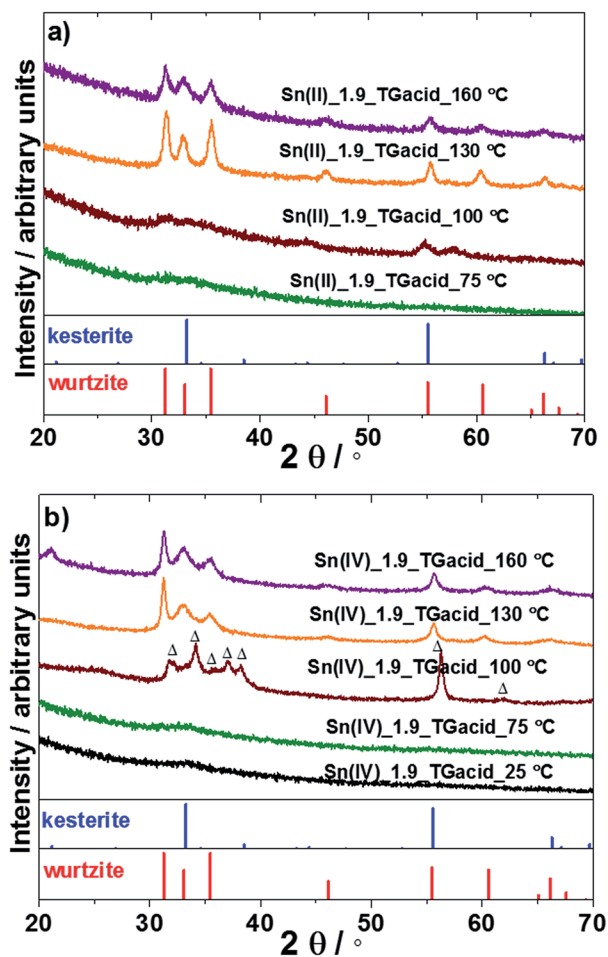
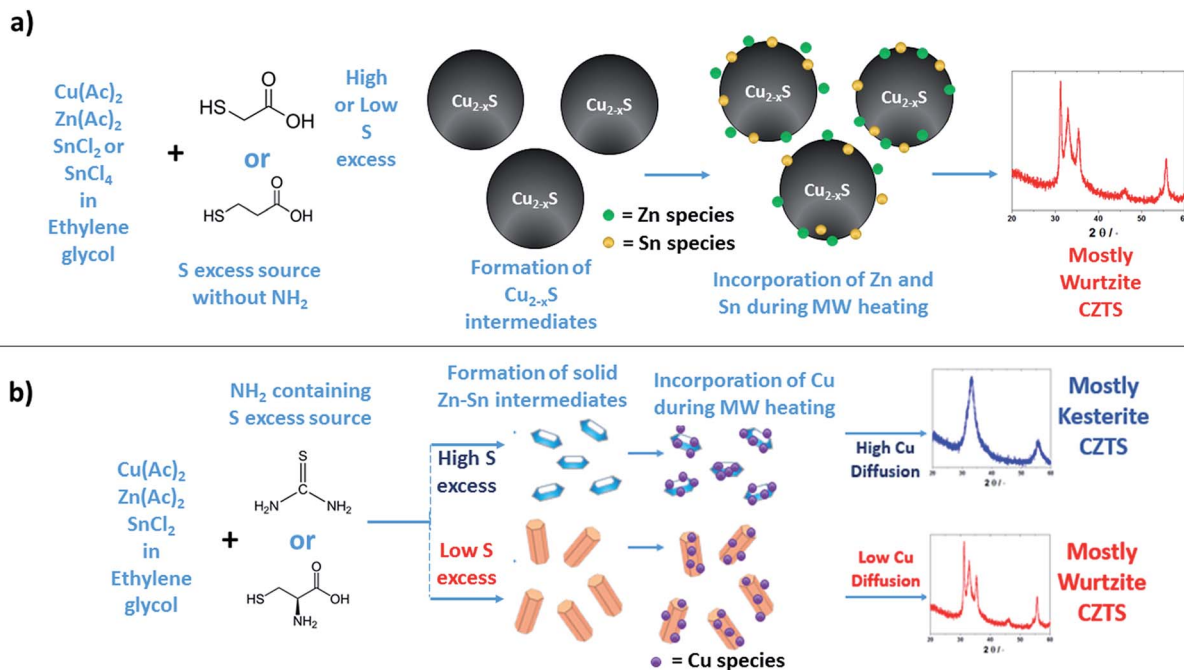


Fig. 8 XRD pattern of the samples  $Cu(II)_{Sn(II)}TGacid_{1.9_T}$  and  $Cu(II)_{Sn(IV)}TGacid_{1.9_T}$ , with  $T$  between 25 and 160 °C. The sample  $Cu(II)_{Sn(II)}TGacid_{1.9_{25}}$  °C did not produce any solid. Peaks labelled as  $\Delta$  are consistent with  $Cu_{2-x}S$  matching the following patterns  $CuS$  – PDF# 00-006-0464,  $Cu_9S_8$  PDF# 00-036-0379, and  $Cu_{39}S_{28}$  PDF# 00-036-0380 (see also Table S7 in the ESI† for the elemental analysis results).

forming. It is also consistent with copper not becoming incorporated into the Zn–Sn intermediate by complexing with thio-urea like Zn(II) and Sn(II) do as would be expected from Pearson's HSAB theory. As the temperature is increased these amino complexes dissociate, allowing copper to react with the Zn–Sn intermediate to form CZTS.

## Summary and conclusions

Scheme 1 is a schematic summary of our findings. Our main conclusion is the existence of two distinct pathways to wurtzite CZTS nanocrystals. One of these (Scheme 1a) is *via* copper sulfide intermediates as previously reported and discussed in the literature.<sup>13,20</sup> In this pathway, the oxidation state of the tin and  $S : M$  ratio does not play a role in determining the phase of the CZTS: it seems that wurtzite CZTS is formed as long as copper sulfides are formed as intermediates. The second pathway (Scheme 1b) is new and involves an intermediate Zn–



**Scheme 1** (a) Reaction scheme for S excess source containing  $\text{NH}_2$  group, according to the S : M variation, leading to kesterite or wurtzite CZTS; (b) reaction scheme for S excess source without  $\text{NH}_2$  group, leading mostly to wurtzite CZTS.

Sn intermediate that appears to form only when the sulfur precursor contains  $-\text{NH}_2$  groups. In this second pathway, the oxidation state of the tin and S : M ratio does play a significant role. The former determines whether the intermediate can form and the latter determines the morphology of the precursor and thus the transformation rate of the precursor to CZTS. The Zn-Sn intermediate forms only when the Sn source is in the +2 oxidation state and does not form when the tin is in +4 oxidation state.

In the new mechanism (Scheme 1b) the first step is the formation of Zn-Sn intermediate precursor particles upon mixing of the reagent solutions. This reaction proceeds even at room temperature. The morphology of these Zn-Sn intermediate particles depends on the S : M ratio. At low thiourea concentration (*i.e.*, S : M = 1.9) large hexagonal prisms form. On the other hand, at higher thiourea concentrations (*i.e.*, S : M = 6.2), dissolution-reconstitution rates will increase and faster localized Ostwald ripening will produce hollow hexagonal plate-like structures.<sup>48-51</sup> The second step is the transformation of the Zn-Sn intermediate precursor to CZTS, in either the wurtzite or the kesterite phase. This transformation requires the diffusion into and reaction of copper with the intermediate. After  $\text{Cu}(\text{II})$  adsorbs on to the Zn-Sn intermediates, the high temperature in the microwave promotes the mixing, interdiffusion, and reaction of the species present in the Zn-Sn intermediate particles and  $\text{Cu}(\text{II})$  ions. The rate of this transformation depends on the morphology of the intermediate. Small, hollow structures promote faster conversion while large hexagonal prisms slow down the transformation. A major consequence of the morphological difference between the products synthesized with S : M = 1.9 and S : M = 6.2 is

that the interdiffusion rate of the elements within the hexagonal prism shaped Zn-Sn intermediate particles (obtained with S : M = 1.9) is slower than the interdiffusion rate in the hollow hexagonal plate-like particles (obtained with S : M = 6.2) (it is easier to diffuse into a small hollow structure with high surface to volume ratio that it is to diffuse into a larger one with low surface to volume ratio). Consequently, the Zn-Sn intermediates prepared with S : M = 1.9 require a higher temperature in order to convert to CZTS. To test this hypothesis, we examined the SEMs of the products whose XRD patterns are shown in Fig. 6 (see Fig. S11 in ESI†). These SEM images show that, indeed, the large hexagonal prisms (S : M = 1.9) still persist at 100 °C with small spherical CZTS particles growing around them while the hollow hexagonal plates (S : M = 6.2) have been completely converted. The slower diffusion rate of Cu into the hexagonal prism shaped large Zn-Sn-intermediate particles (obtained with S : M = 1.9) slows the transformation of the intermediate to CZTS. This slow transformation leads to the formation of the metastable wurtzite phase.

## Conflicts of interest

There are no conflicts to declare.

## Acknowledgements

This research was supported by Environmental and Natural Resources Trust Fund (ENRTF) from State of Minnesota. Part of this work was carried out in the College of Science and Engineering Characterization Facility, University of Minnesota,

which has received capital equipment funding from the NSF through the UMN MRSEC program under Award Number DMR-1420013.

## Notes and references

- M. A. Green, *J. Mater. Sci.: Mater. Electron.*, 2007, **18**, 15–19.
- C. A. Wolden, J. Kurtin, J. B. Baxter, I. Repins, S. E. Shaheen, J. T. Torvik, A. A. Rockett, V. M. Fthenakis and E. S. Aydil, *J. Vac. Sci. Technol.*, 2011, **29**, 30801–30815.
- M. A. Green, K. Emery, Y. Hishikawa, W. Warta and E. D. Dunlop, *Prog. Photovoltaics*, 2015, **23**, 1–9.
- H. Liu, V. Avrutin, N. Izyumskaya, Ü. Özgür and H. Morkoç, *Superlattices Microstruct.*, 2010, **48**, 458–484.
- C. Steinhagen, M. G. Panthani, V. Akhavan, B. Goodfellow, B. Koo and B. A. Korgel, *J. Am. Chem. Soc.*, 2009, **131**, 12554–12555.
- T. J. Huang, X. Yin, G. Qi and H. Gong, *Phys. Status Solidi RRL*, 2014, **8**, 735–762.
- A. D. Collord and H. W. Hillhouse, *Chem. Mater.*, 2015, **27**, 1855–1862.
- J. Kim, H. Hiroi, T. K. Todorov, O. Gunawan, M. Kuwahara, T. Gokmen, D. Nair, M. Hopstaken, B. Shin, Y. S. Lee, W. Wang, H. Sugimoto and D. B. Mitzi, *Adv. Mater.*, 2014, **26**, 7427–7431.
- A. Khare, B. Himmetoglu, M. Johnson, D. J. Norris, M. Cococcioni and E. S. Aydil, *J. Appl. Phys.*, 2012, **111**, 083707–083715.
- S. Chen, A. Walsh, Y. Luo, J. H. Yang, X. G. Gong and S. H. Wei, *Phys. Rev. B: Condens. Matter Mater. Phys.*, 2010, **82**, 1–8.
- H. Jiang, P. Dai, Z. Feng, W. Fan and J. Zhan, *J. Mater. Chem.*, 2012, **22**, 7502–7506.
- S. Schorr, H.-J. Hoebler and M. Tovar, *Eur. J. Mineral.*, 2007, **19**, 65–73.
- M. D. Regulacio, C. Ye, S. H. Lim, M. Bosman, E. Ye, S. Chen, Q.-H. Xu and M.-Y. Han, *Chem.–Eur. J.*, 2012, **18**, 3127–3131.
- X. Lu, Z. Zhuang, Q. Peng and Y. Li, *Chem. Commun.*, 2011, **47**, 3141–3143.
- A. Singh, H. Geaney, F. Laffir and K. M. Ryan, *J. Am. Chem. Soc.*, 2012, **134**, 2910–2913.
- X. Lin, J. Kavalakkatt, K. Kornhuber, D. Abou-Ras, S. Schorr, M. C. Lux-Steiner and A. Ennaoui, *RSC Adv.*, 2012, **2**, 9894–9898.
- Y. Wang, M. Wei, F. Fan, T. Zhuang, L. Wu, S. Yu and C. Zhu, *Chem. Mater.*, 2014, **26**, 5492–5498.
- Z. Li, A. L. K. Lui, K. H. Lam, L. Xi and Y. M. Lam, *Inorg. Chem.*, 2014, **53**, 10874–10880.
- Y.-H. Lin, S. Das, C.-Y. Yang, J.-C. Sung and C.-H. Lu, *J. Alloys Compd.*, 2015, **632**, 354–360.
- M. Li, W.-H. Zhou, J. Guo, Y.-L. Zhou, Z. Hou, J. Jiao, Z. Zhou, Z. Du and S. Wu, *J. Phys. Chem. C*, 2012, **116**, 26507–26516.
- U. V. Ghorpade, M. P. Suryawanshi, S. W. Shin, C. W. Hong, I. Kim, J. H. Moon, J. H. Yun, J. H. Kim and S. S. Kolekar, *Phys. Chem. Chem. Phys.*, 2015, **17**, 19777–19788.
- G. Gabka, P. Bujak, M. Gryszel, A. Ostrowski, K. Malinowska, G. Z. Zukowska, F. Agnese, A. Pron and P. Reiss, *Chem. Commun.*, 2015, **51**, 12985–12988.
- H. Guan, H. Hou, F. Yu and L. Li, *Mater. Lett.*, 2015, **159**, 200–203.
- Y. Park, H. Jin, J. Park and S. Kim, *CrystEngComm*, 2014, **16**, 8642–8645.
- H. W. Hillhouse and M. C. Beard, *Curr. Opin. Colloid Interface Sci.*, 2009, **14**, 245–259.
- Q. Guo, H. W. Hillhouse and R. Agrawal, *J. Am. Chem. Soc.*, 2009, **131**, 11672–11673.
- B. D. Chernomordik, A. E. Béland, D. D. Deng, L. F. Francis and E. S. Aydil, *Chem. Mater.*, 2014, **26**, 3191–3201.
- B. D. Chernomordik, P. M. Ketkar, A. K. Hunter, A. E. Béland, D. D. Deng and E. S. Aydil, *Chem. Mater.*, 2016, **28**, 1266–1276.
- R. Mainz, A. Singh, S. Levchenko, M. Klaus, C. Genzel, K. M. Ryan and T. Unold, *Nat. Commun.*, 2014, **5**, 3133.
- W.-C. Yang, C. K. Miskin, C. J. Hages, E. C. Hanley, C. Handwerker, E. A. Stach and R. Agrawal, *Chem. Mater.*, 2014, **26**, 3530–3534.
- X. Lin, J. Kavalakkatt, A. Ennaoui and M. C. Lux-Steiner, *Sol. Energy Mater. Sol. Cells*, 2015, **132**, 221–229.
- M. Himmrich and H. Haeuselner, *Spectrochim. Acta, Part A*, 1991, **47**, 933–942.
- A.-J. Cheng, M. Manno, A. Khare, C. Leighton, S. A. Campbell and E. S. Aydil, *J. Vac. Sci. Technol.*, 2011, **29**, 051203–051213.
- M. Y. Valakh, O. F. Kolomys, S. S. Ponomaryov, V. O. Yukhymchuk, I. S. Babichuk, V. Izquierdo-Roca, E. Saucedo, A. Perez-Rodriguez, J. R. Morante, S. Schorr and I. V. Bodnar, *Phys. Status Solidi RRL*, 2013, **7**, 258–261.
- R. Ahmad, M. Brandl, M. Distaso, P. Herre, E. Spiecker, R. Hock and W. Peukert, *CrystEngComm*, 2015, **17**, 6972–6984.
- L. Arora, P. Gupta, N. Chhikara, O. P. Singh, N. Muhunthan, V. N. Singh, B. P. Singh, K. Jain and S. Chand, *Appl. Nanosci.*, 2015, **5**, 163–167.
- Y. Wang, X. Jiang and Y. Xia, *J. Am. Chem. Soc.*, 2003, **125**, 16176–16177.
- S. H. Ng, S. Y. Chew, D. I. Dos Santos, J. Chen, J. Z. Wang, S. X. Dou and H. K. Liu, *Chem.–Asian J.*, 2008, **3**, 854–861.
- J. Das, I. R. Evans and D. Khushalani, *Inorg. Chem.*, 2009, **48**, 3508–3510.
- D. Jayalakshmi and J. Kumar, *Cryst. Res. Technol.*, 2006, **41**, 37–40.
- M. Lydia Caroline and S. Vasudevan, *Curr. Appl. Phys.*, 2009, **9**, 1054–1061.
- J. E. Cassidy, W. Moser, J. D. Donaldson, A. Jelen and D. G. Nicholson, *J. Chem. Soc. A*, 1970, 173–175.
- P. G. Harrison, B. J. Haylett and T. J. King, *Inorg. Chim. Acta*, 1983, **75**, 259–264.
- A. D. Burrows, A. S. Donovan, R. W. Harrington and M. F. Mahon, *Eur. J. Inorg. Chem.*, 2004, 4686–4695.
- J. Hilbert, C. Näther, R. Wehrich and W. Bensch, *Inorg. Chem.*, 2016, **55**, 7859–7865.
- R. G. Pearson, *J. Chem. Educ.*, 1968, **45**, 581–587.

- 47 J. Li, M. Bloemen, J. Parisi and J. Kolny-Olesiak, *ACS Appl. Mater. Interfaces*, 2014, **6**, 20535–20543.
- 48 S. A. Morin, A. Forticaux, M. J. Bierman and S. Jin, *Nano Lett.*, 2011, **11**, 4449–4455.
- 49 R. M. Dziejczak, A. L. Gillian-Daniel, G. M. Petersen and K. J. Martinez-Hernandez, *J. Chem. Educ.*, 2014, **91**, 1710–1714.
- 50 H. Yu, J. Yu, S. Liu and S. Mann, *Chem. Mater.*, 2007, **19**, 4327–4334.
- 51 X. W. Lou, L. A. Archer and Z. Yang, *Adv. Mater.*, 2008, **20**, 3987–4019.